In-situ spectroelectrochemical study of highly active Ni-based foam electrocatalysts for hydrogen evolution reaction

Antony Bazan-Aguilar [a,b], Gonzalo García [c,*], Elena Pastor [c], José Luis Rodríguez [c], Angélica María Baena-Moncada [a,*]

[a] *Laboratorio de Investigación de Electroquímica Aplicada, Facultad de Ciencias, Universidad Nacional de Ingeniería, 210 Túpac Amaru Ave., 15333 Lima, Peru*
[b] *Universidad Tecnológica del Perú, 265 Arequipa Ave., 15046 Lima, Peru*
[c] *Instituto Universitario de Materiales y Nanotecnología, Departamento de Química, Universidad de La Laguna (ULL), PO Box 456, 38200, La Laguna, Santa Cruz de Tenerife, España*

A B S T R A C T

Green hydrogen is a valuable energy source able to overcome the environmental issues generated by fossil fuel consumption. In this regard, large-scale production of green hydrogen could be achieved by anion exchange membrane water electrolyzer (AEMWE). However, highly electroactive, and low-cost catalysts for hydrogen evolution reaction (HER) are critical to executing AEMWE. With this end in view, a straightforward route is revealed to improve the catalytic performance toward the HER of commercial and low-cost Ni foam electrodes.

Indeed, an oxyhydroxide nickel-based surface was obtained after a facile and low-cost anhydrous etching procedure of the raw material. The novel catalyst reveals an onset potential for the HER of ca. 10.0 mV (vs. RHE), which is very close to the thermodynamic value, and an increment of the catalytic efficiency towards the HER. Furthermore, differential electrochemical mass spectrometry (DEMS) and Raman spectroelectrochemistry (Raman-SEC) were employed to get insight into the reaction kinetics and mechanism of the HER at catalysts in alkaline medium.

1. Introduction

Green hydrogen, obtained by electrolysis in alkaline media, stands out by a high energy density, c.a. three-times gasoline energy density (MJ kg^{-1}), and zero-emission consumption [1]. In this sense, green hydrogen is regarded as the future energy carrier in replacement of fossil fuels [1,2]. As well, its promising applications as an energy storage vector of renewable energy sources e.g., solar and wind energy [3,4], or high-purity reagent for industrial synthesis [5], have stimulated the design of efficient and scalable production strategies [5,6].

Alkaline (AWE), polymer exchange membrane (PEMWE), and anion exchange membrane (AEMWE) water electrolysis are the main strategies to obtain green hydrogen [7–12]. AWE employs abundant and sustainable non-precious metal as catalysts, but is unable to produce pressurized hydrogen and shows low efficiency for motorized applications [7]. On the other hand, PEMWE reveals higher efficiencies than AWE and can be fed with deionized water. However, its scale-up is restricted owing to the low-relative abundance of highly active metals used as catalysts. Either oxygen evolution reaction (OER) or hydrogen evolution

reaction (HER) on PEMWE are limited by this fact, e.g., IrO$_2$||Pt benchmarking couple of 1.57 V at 10 mA cm^{-2} [4,6,13,14]. Furthermore, fluorine-based polymers are used as membrane in PEMWE configuration, and the production implies an environmental impact due to the fluorocarbon gas emission [7,14]. In this scenario, AEMWE technology includes the advantages of AWE (non-noble metal-based electrocatalysts) and PEMWE (production of ultrapure and pressurized H$_2$) [7,14]. Additionally, AEMWE employs a low-cost membrane free of fluorine-based polymers [7].

Among the different approaches, the design of non-noble metal-based electrocatalysts is the most reported method to overcome the issue discussed above in both half-reactions [4,15–18]. Concerning HER, Ni-based materials are highlighted by their promising performance and scalability [7,18–20]. Both characteristics can conquer poor availability and low efficiency to water dissociation of Pt-based catalysts in alkaline media [21–23].

Precisely, remarkable activity, great reaction rate, high relative abundance on earth, and low cost are reported to Ni-based catalysts, whereby, they have gained considerable attention to replace Pt-based

---

materials [24–26]. For instance, the insertion of $Ni(OH)_2$-nanospheres onto Pt electrode reveals an overpotential (η_{HER}) of 52 mV at -4.0 mA cm^{-2} lower than Pt electrode (70 mV) in 0.1 M KOH [22]. As well, nickel nanowires (Ni-NWs) report a η_{HER} of 47 mV while, NiCu nanosheets register a value of 127 mV at -10 mA cm^{-2} in an alkaline solution [21].

In the last years, Ni-foam-based catalysts have recorded an outstanding performance owing to their high density of active sites and improved hydrogen gas diffusion [13,27]. For example, Ni/NiO monolithic electrodes obtained by acid-promoted activation of Ni foam surface at 120 °C register a η_{HER} of 160 mV at -10 mA cm^{-2} in alkaline medium [28], whereas NiFe-based electrocatalysts on nickel foam achieve an overpotential of 87 mV at -10 mA cm^{-2} [29] lower than pure Ni foam, c.a., 300 mV in 1.0 KOH [30,31].

Despite these promising results, a highly active Ni-based electrocatalyst able to be commercially competitive is not registered yet. Furthermore, not only the synthetic route to obtain them but also a complete understanding of their electrochemistry performance toward the HER is a scientific challenge nowadays.

Hence, herein we report an effortless and low-cost route to obtain highly active Ni foam-based electrocatalysts toward the HER in alkaline media from commercial and low-cost Ni-foam material. To achieve a depth understanding of the kinetics and reaction mechanism, in-situ Raman spectroelectrochemistry (Raman-SEC) and differential electrochemical mass spectrometry (DEMS) were employed.

2. Experimental procedure

2.1. Two-step anhydrous etching route

Commercial nickel foam (NiF, 2.0 mm of thickness, purity $\geq 99.8\%$, 21.7 cm^2 g^{-1}, TMAX) was cut into pieces of 2.0×2.5 cm^2, cleaned with acetone ($\geq 99.5\%$, Merck), and dried at room temperature.

Each piece of NiF was activated by two-step ultrasound treatment in (i) 3.0 M HCl ($> 99.0\%$, Merck) [28,32,33], and (ii) absolute ethanol (99.5%, Merck) as dehydrating agent during 15 min per step. Then, the samples were dried at 90 °C for 8 h, and the anhydrous etched electrodes were labeled as NiF$_A$.

2.2. Physicochemical characterization

Morphology and surface analysis of NiF and NiF$_A$ were carried out by scanning electron microscope (SU8230, Hitachi) equipped with an X-ray energy dispersive spectrometer (EDX) (Oxford X-MAX spectrometer).

Diffraction patterns were recorded from 10° to 100° (2θ) using an incidence X-ray beam ($\lambda = 0.15406$ nm) emitted by Cu-K$_\alpha$ cathode at 40 kV and 20 mA in a PANalytical X'Pert-Pro diffractometer. Deconvolution of the main diffraction peaks was performed by non-linear mathematical fitting with a Voigt function [34].

Attenuated total reflectance infrared spectroscopy (ATR-FTIRS) achieved from 500 to 4500 cm^{-1} was carried out in a Bruker IFS 66/S infrared spectrometer. Detailed analysis of infrared bands was performed by the determination of reflectance ratio, R_{NiFA}/R_{NiF}, where R_{NiFA} and R_{NiF} are the reflectance of NiF$_A$ and NiF electrodes, respectively.

Raman spectra of nickel-based electrodes were acquired by an incident laser beam of 532 nm and a SPELEC Raman spectrometer (Metrohm-Dropsens). Raman signal deconvolution was carried out by extracting the fluorescence background through a mathematical treatment using the asymmetric least squares method [35–37].

2.3. Electrochemical measurements

Electrochemical measurements were performed in a three-electrode cell, with a reversible hydrogen electrode (RHE), a glassy carbon electrode (GC), and a piece of NiF or NiF$_A$ electrode as reference electrode (RE), counter electrode (CE), and working electrode (WE), respectively. Aqueous 0.1 M NaOH electrolyte was prepared from high-purity reagents (Puriss p.a., Honeywell) and ultra-pure water (Millipore Milli-Q gradient A10 system, 18.2 MΩ cm, 2 ppb total organic carbon). Argon (Air Liquide, N50) was used to deoxygenate all solutions. PC Autolab potentiostat-galvanostat PGSTAT30 was employed to perform cyclic voltammetry (CVs) between -0.10 and 0.90 V at 0.02 V s^{-1} and chronopotentiometry tests at -10.0 mA cm^{-2} during 3600 s in deoxygenated 0.1 M NaOH aqueous solution.

2.3.1. DEMS set-up

Gaseous and volatile species produced at the working electrode were continuously detected by differential electrochemical mass spectrometry (DEMS). The set-up configuration developed for the study of the Ni foam samples has the same working principle as the online electrochemical mass spectrometry developed by Guillén-Villafuerte et al. [38]. The DEMS configuration consists of a commercial mass spectrometer (Omnistar™, Pfeiffer) with a PTFE capillary (Supelco) as an inlet and a small porous PTFE membrane (Scimat) located on the tip. The capillary was fixed in a carbon disk with a hole in the middle. Then, a small piece of NiF (2.0 mg) or NiF$_A$ (1.2 mg) was introduced into the hole of the carbon disk and pressed against the PTFE membrane. After that, mass spectrometry cyclic voltammograms (MSCVs) and mass current transients (MSCTs) ($m/z = 2$) can be acquired simultaneously with the corresponding CVs and current transients (CTs). MSCVs and CVs were recorded between -0.25 and 0.25 V at 1.0 mV s^{-1} in 0.1 M NaOH aqueous solution [38].

2.3.2. In-situ Raman spectroelectrochemistry setup

A corrosion-like three-electrode cell was set-up to perform in-situ Raman spectroelectrochemistry (Raman-SEC). Briefly, a circular piece of NiF (8.3 mg) or NiF$_A$ (7.0 mg) (WE) connected with a gold wire is situated at 2 and 5 mm above the RE (RHE) and CE (glassy carbon disc) in an electrochemical Teflon cell, respectively (Fig. 1). The Raman laser probe is located at c.a. 7 mm above the WE and in-situ Raman-SEC spectra were recorded from 0.5 to -0.3 V (vs. RHE) with 0.1 V of potential step during 50 s [39].

3. Results and discussion

3.1. Two-step anhydrous etching route

The classical etching process involves the Ni-based electrode soaking in an aqueous acid solution, e.g., HCl, H_2SO_4, HNO_3, CH_3COOH at room or higher temperatures [32,40,41]. This uncontrolled etching process removes the external NiO and dissolves the internal metallic surface as a Ni^{2+} aqueous solution [32,40]. Additionally, a second soaking step is usually employed to clean the Ni surface from organic molecules; however, fragile mechanical structures and Ni surface oxide species are frequently achieved [42–44].

Herein, we report a two-step anhydrous etching route assisted by ultrasound. Briefly, Ni foam pieces are soaked in pure acetone to remove organic impurities. The cleaned samples are treated in 3 M HCl in an ultrasound bath for 15 min (1st step). Then, the samples are transferred to a flask containing absolute ethanol for 15 min (2nd step). Finally, the etched samples are dried at 90 °C for 8 h.

In this way, the effect of an aqueous environment during the synthetic route is minimized by an effortless and controlled route to obtain a metallic nickel surface with high roughness, crystallinity, and catalytic performance toward the HER.

3.2. Physicochemical characterization

3.2.1. Scanning electron microscopy (SEM) analysis

NiF shows an interconnected three-dimensional network formed by macropores ranging from 50 to 500 μm (Fig. 2a). Specifically, a pore size
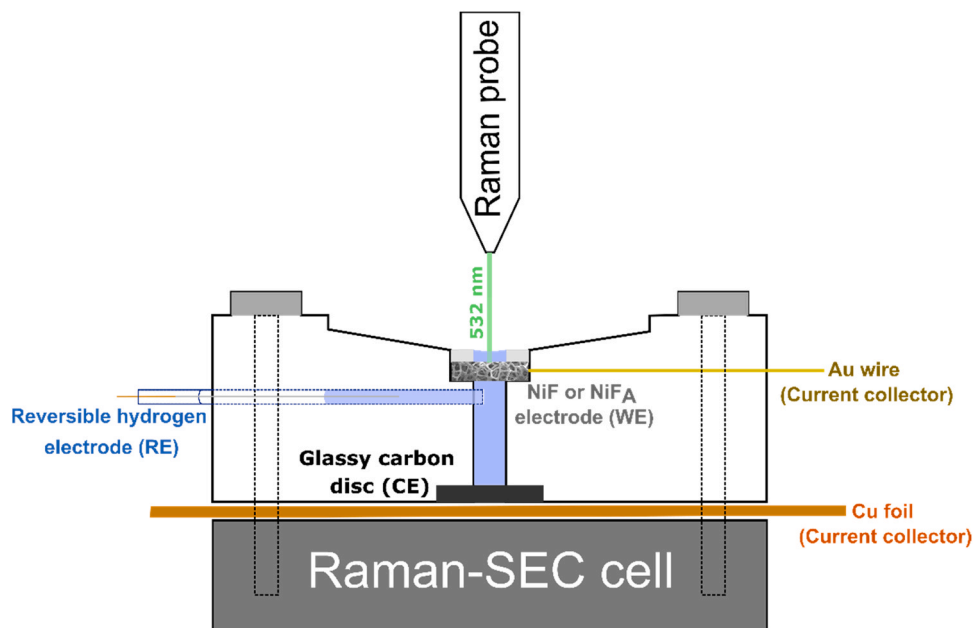
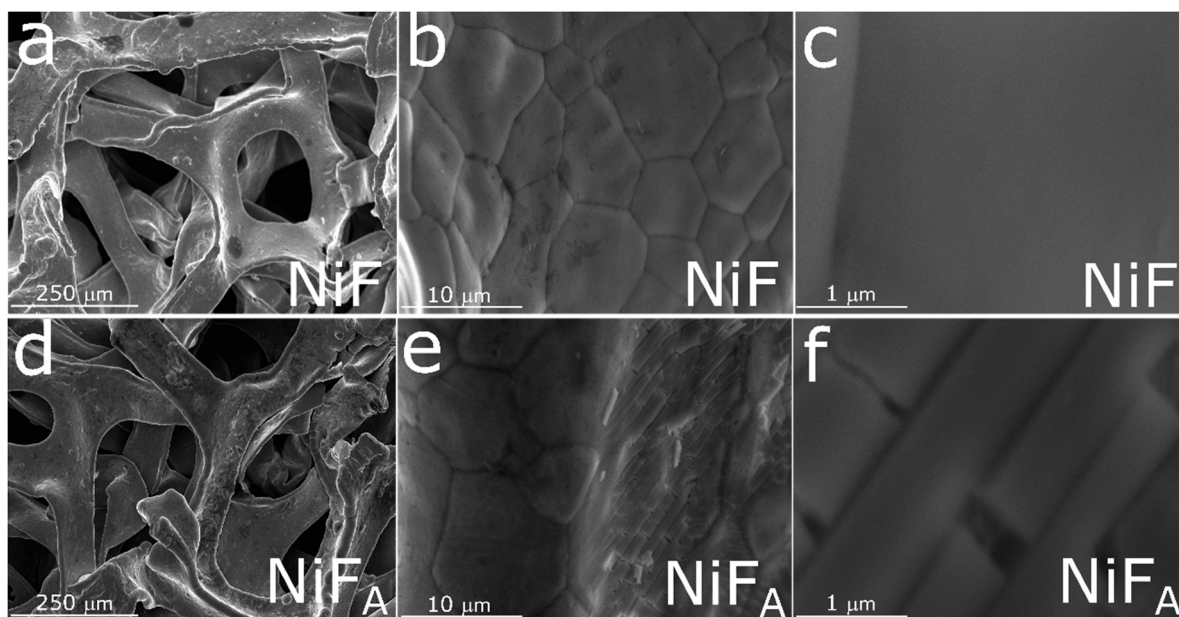**Fig. 1.** Scheme of the in-situ Raman spectroelectrochemical cell.

Fig. 2. SEM images of NiF (a, b, c) and NiF$_A$ (d, e, f) electrodes.

distribution analysis reveals a pore average size of ca. 230 μm. Its surface is formed by micrometric polygonal grains (Fig. 2b), where each one displays a low roughness surface (Fig. 2c). Both hollow and interconnected branches do not affect the mechanical stability of the metallic foam.

The appearance of NiF material shifts from gray to yellow color after the anhydrous etching process. The etched surface of the NiF$_A$ electrode possesses an interconnected macropores network (Fig. 2d) with a similar pore average size to that observed for NiF (Fig. 2e). Furthermore, Fig. 2f reveals internal and regular fractures with rectangular geometry, which suggests an increase in the surface area.

Accordingly, anhydrous etching by ultrasound appears to dissolve the passivated bilayer surface (PBS) of NiF [28,33,42]. In this sense, PBS grows on the metallic nickel foam surface during sintering and prolonged exposure to air, and it is usually composed of Ni(OH)$_2$ and NiO

species [37,40,42], which may be removed by acid treatment according to:

$$Ni_{bulk}/NiO_{(s)}\Big/Ni(OH)_{2(s)} + 4HCl_{(ac)} \longrightarrow Ni_{bulk} + 2NiCl_{2(ac)} + 3H_2O_{(l)} \quad (1)$$
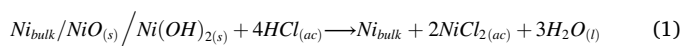
where, Ni_{bulk} is the internal metallic surface, and $NiO_{2(s)}/Ni(OH)_{2(s)}$ form the PBS. The growth of this surface oxide layer is self-controlled by the formation of hydroxide species [37,43]. In-situ X-ray scattering measurements at Ni(111) monocrystal in 1 M KOH solution suggest that its surface is coated by a very thin NiO film of 2 – 4 layers of thickness. Also, the external NiO atomic layer forms an external hydroxyl layer which expands owing to the exposition to water in the air [43].

3.2.2. X-ray diffraction analysis
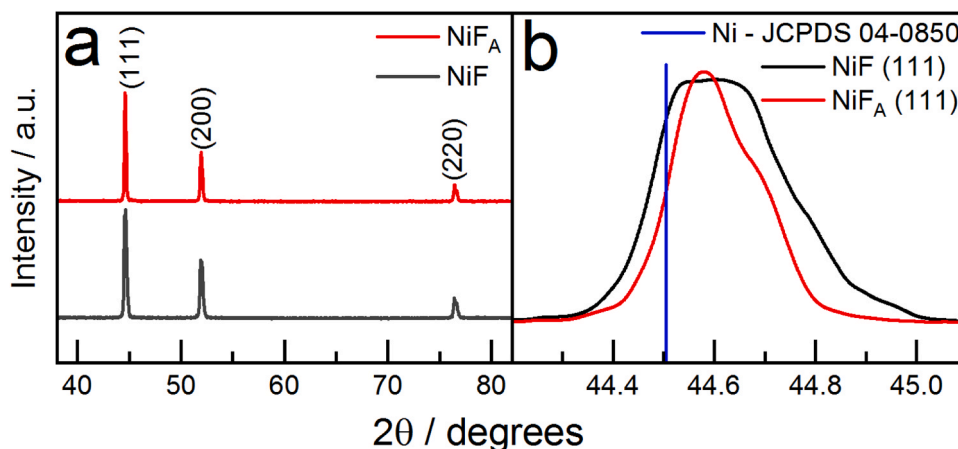Fig. 3a displays X-ray diffraction patterns of NiF and NiF$_A$ materials.

Fig. 3. Diffraction patterns of NiF and NiF$_A$ electrodes (a) and zoom of the Ni (111) crystallographic plane (b).

Both samples depict intense signals at $2\theta = 44.5°$, 52.0°, and 76.5° corresponding to (111), (200), and (220) crystal planes of Ni (JCPDS no. 04–850) [37,42].

Therefore, both materials reveal typical XRD spectra of fcc-Ni structure with a single crystalline phase. Nevertheless, amorphous Ni oxide species at the surface are not discarded [45,46].

In this sense, Fig. 3b reveals a slight displacement of the X-ray pattern to low diffraction angles after the anhydrous etching, which suggests an expansion of the crystalline lattice.

Furthermore, NiF$_A$ shows a full width at half maximum (FWHM) value smaller than NiF at the main diffraction planes, which points out the higher crystallinity degree of the NiF$_A$ material (Table 1) [34,45].

Therefore, SEM images and X-ray analysis reveal that NiF$_A$ surface shows higher roughness than NiF (Figs. 2c and 2f) and crystallinity degree after removal of the external NiO-based layer [40,42,43].

3.2.3. Infrared spectroscopy analysis

Fig. 4 shows the IR spectrum obtained as R_{NiFA}/R_{NiF} where R_{NiFA} and R_{NiF} are the reflectance measured at the NiF$_A$ and the NiF materials, respectively. In this spectrum, positive bands correspond to the loss of species after the anhydrous etching [47]. Accordingly, positive bands are discernable at 670, 855, 960, 1085, 1225, 1410, 1460, 1535 and 1650 cm^{-1}. The assignment of all these bands is summarized in Table 2.

The positive feature around 1650 cm^{-1} is due to the OH bending mode of surface water and only one IR-active mode of α-Ni(OH)$_2$ is visible as a broad band at a lower wavenumber than 650 cm^{-1}. A sharp peak at 855 cm^{-1} and a weak one at ca. 1085 cm^{-1} are discerned and attributed to combinations of α-Ni(OH)$_2$ bands, and OH bending modes of lattice OH are observed between 1350 and 1600 cm^{-1} [25,33,37,42,47–49]. The sharp feature located at 960 cm^{-1} and broad ones between 1100 and 1300 cm^{-1} are presumably ascribed to stretching modes of incorporated carbonate and/or sulfate ions in the interlayer space of the commercial NiF material and/or hydrocarbons onto the NiF surface [37,42,50,51]. Therefore, it is proved that a great amount of intercalated and surface species is lost after anhydrous etching.

3.2.4. Raman spectroscopy analysis

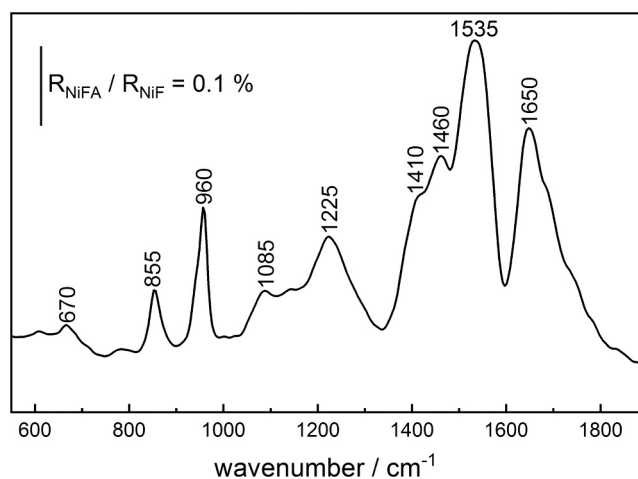The fluorescence background [35,36] and the artifact dispersion

Fig. 4. FTIR spectrum (R_{NiFA}/R_{NiF}) of lost species after the anhydrous etching. The reference spectrum was taken at the R_{NiF} electrode.

Table 2
Main vibrational modes recorded by IR spectroscopy.

Frequency / cm^{-1}	Assignment	[Ref.]
≤ 670	$(O-H)$ bending mode of α-Ni(OH)$_2$ lattice	[42,49]
855	combination Ni(OH)$_2$ lattice mode	[37,42]
960	stretching modes of SO_4^{2-} stretching modes of CO_3^{2-}	[37,42,50,51]
1085	combination Ni(OH)$_2$ lattice mode	[37,42,50]
1100–1300	stretching modes of SO_4^{2-} stretching modes of CO_3^{2-}	[37,42,50,51]
1410	O−H bending modes of lattice OH	[37,42]
1460		
1535		[42,49]
1650	O−H bending mode of surface water	[25,33,42]

Table 1
Crystallographic parameters for NiF and NiF$_A$ electrodes.

Crystallographic plane ($h\,k\,l$)	Diffraction angle 2θ / degrees			Interplanar distance d_{hkl} / Å		FWHM / degrees	
	JCPDS 04–0850	NiF	NiF$_A$	NiF	NiF$_A$	NiF	NiF$_A$
(111)	44.51	44.61	44.57	20.29	20.31	0.28	0.14
(200)	51.84	51.97	51.93	17.58	17.60	0.32	0.18
(220)	76.37	76.52	76.44	12.44	12.45	0.42	0.18

peak at 2322.5 cm^{-1} were removed from all Raman spectra before the analysis [37]. Fig. 5 shows Raman spectra obtained for NiF and NiF$_A$ materials. The anhydrous etching eliminates a great amount of Raman signals, which agrees with FTIRS results.

All Raman-active bands developed at the NiF electrode are correlated to α-Ni(OH)$_2$ species (Table 3 depicts peak assignments). The broad band at ca. 410 cm^{-1} is related to lattice modes, while the sharp peak at 720 cm^{-1} and 1030 cm^{-1} are associated with second-order transitions [37,42]. In agreement with FTIRS results, the broadband at ca. 1410 cm^{-1} is related to internal OH bending modes of lattice OH. In addition, a very sharp peak at 1550 cm^{-1} (second magnetic mode of Ni-O lattice) is associated to surface nickel oxide species (NiO) produced in the presence of oxygen in the air [37,42,52]. The so-called C-band ($v_{C=C}$) is composed of a shoulder at ca. 1915 cm^{-1} and the main peak at 2100 cm^{-1}, while the band at ca. 2880 cm^{-1} is ascribed to the stretching modes of C-H species [53,54].

In this context, commercial nickel foam is produced by nickel plating into a reticular polymer substrate (polyurethane foam, Pluronic F127, etc.) and subsequently, the compound is sintered under a controlled atmosphere at high temperatures [50,55]. Furthermore, nickel tetra-carbonyl (Ni(CO)$_4$) is used as a precursor, and therefore sulfur and carbon species are the main impurities at commercial Ni foam ($\geq$ 99.8%) [50,56]. In this sense, strong Raman-active modes registered at 2100 cm^{-1} are associated with C(sp^2) species at the catalyst surface [53,54].

The last indicates the presence of hydrocarbons on the NiF surface. Then, the broad band peaking at 3460 cm^{-1} is related to the O-H stretching mode from the α-Ni(OH)$_2$ lattice and/or adsorbed water [37,42].

On the other hand, the anhydrous etching fully removes adsorbed hydrocarbon and surface water species, and partially eliminates internal OH from the lattice. Therefore, only four main Raman-active modes at 430, 1030, 1420, and 1550 cm^{-1} are detected, which indicate a NiF$_A$ surface mainly formed by oxy/hydroxide nickel species [57,58]. It is important to remark on the presence of higher Raman shift values of lattice modes (around 430 and 1420 cm^{-1}) at NiF$_A$ in comparison to NiF, which indicates a contraction of the surface lattice after the etching treatment.

3.3. Electrochemical measurements

3.3.1. Cyclic Voltammetry

Fig. 6a displays the cyclic voltammograms for NiF (black line: multiplied by five) and NiF$_A$ (red line) electrodes in alkaline media. Both materials develop similar voltammetric profiles; however, a great rise in
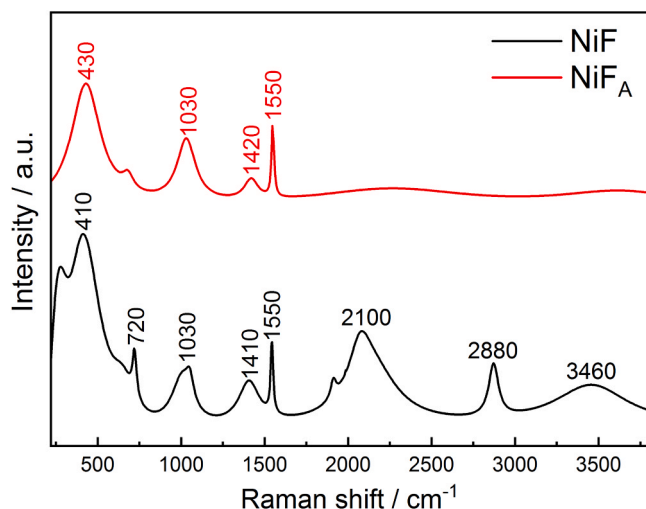
Fig. 5. *ex-situ* Raman spectra of NiF (black line) and NiF$_A$ (red line) electrodes.

Table 3

Assignation of most important active Raman signals observed at NiF and NiF$_A$ catalysts in presence of air and 0.1 M NaOH.

Raman signal / cm^{-1}				Assignation	Vibration mode	Reference
Air		NaOH				
NiF	NiF$_A$	NiF	NiF$_A$			
410	430	445	430	Ni-OH	Acoustic lattice phonon of α-Ni(OH)$_2$	[42]
720	–	–	–	Ni-O	Transversal optical phonon 2 P (TO)$_{NiO}$	[57,74,79]
1030	1030	1030	1050	Ni-OH	Second-order lattice mode of α-Ni(OH)$_2$	[42]
–	–	1220	1235	ONi-OH	γ-NiOOH lattice mode	[26,69]
1410	1420	1400	1400	Ni-O-H	Bending mode of Ni(OH)$_2$ lattice	[37,42]
1550	1550	1545	1540	Ni-O	Second magnetic mode of air formed NiO	[37,42,74]
–	–	1650	1650	H-O-H	Bending mode of layer water (δ_{H_2O})	[70,71]
1915 2100	– –	– –	– –	C=C	Stretching mode ($\nu_{C=C}$)	[53,73]
–	–	2450	–	Ni-O	4th Magnetic mode of NiO ($4M_{NiO}$)	[58,74]
2880	–	–	–	C-H	Stretching mode (ν_{C-H})	[37,50]
–	–	3250	3200	O-H	Symmetric stretching mode (ν_{s,H_2O})	[70,71]
3460	–	3430	3425	O-H	Asymmetric stretching mode (ν_{as,H_2O})	[70,71]
–	–	3600	3625	O-H (H$_2$O)	Stretching mode of the electrolyte (OH$^-$)	[72,73]

the current density is observed after the anhydrous etching. Indeed, an increment of ca. 10% of the whole current (capacitive and faradaic current) is observed. The last is in complete agreement with the observed in Fig. 2f, in which an increase of the active surface area was discerned.

Additionally, in the positive-going scan direction, a small but visible anodic peak appears for NiF$_A$, which can be associated with the reversible formation of α-Ni(OH)$_2$. The last agrees with FTIR (Fig. 4) and Raman (Fig. 5) analysis, in which surface oxygenated species are lost and, consequently, a higher density of active sites are available after the anhydrous etching [59].

The anodic region between 0.2 and 0.6 V is labeled as the Ni(II) region and involves two electrochemical processes, mainly [40,43,63]. The first one is associated with metallic nickel oxidation to NiO$_x$ and α-Ni(OH)$_2$ from 0.2 to 0.4 V [38,41,61], while the second region is ascribed to the thickens chemical modification of NiO$_x$ / α-Ni(OH)$_2$ layer [43,63].

Hence, Fig. 6a shows low anodic currents for NiF regarding both processes mentioned above, which indicate a passivated surface and a lower density of metallic active sites than the etched electrode. NiF$_A$ anodic profile reveals two peaks c.a. 0.2 and 0.5 V (vs RHE) associated with the processes mentioned above and, particularly, the second peak shows the formation of a novel NiO$_x$ /α-Ni(OH)$_2$ layer on the etched metallic surface.

3.3.2. Differential Electrochemical Mass Spectrometry (DEMS)

It is well known that the kinetics and mechanistic parameters of the HER at non-noble materials are quite difficult to obtain from faradaic currents due to the overlap of by-side reactions such as surface oxides
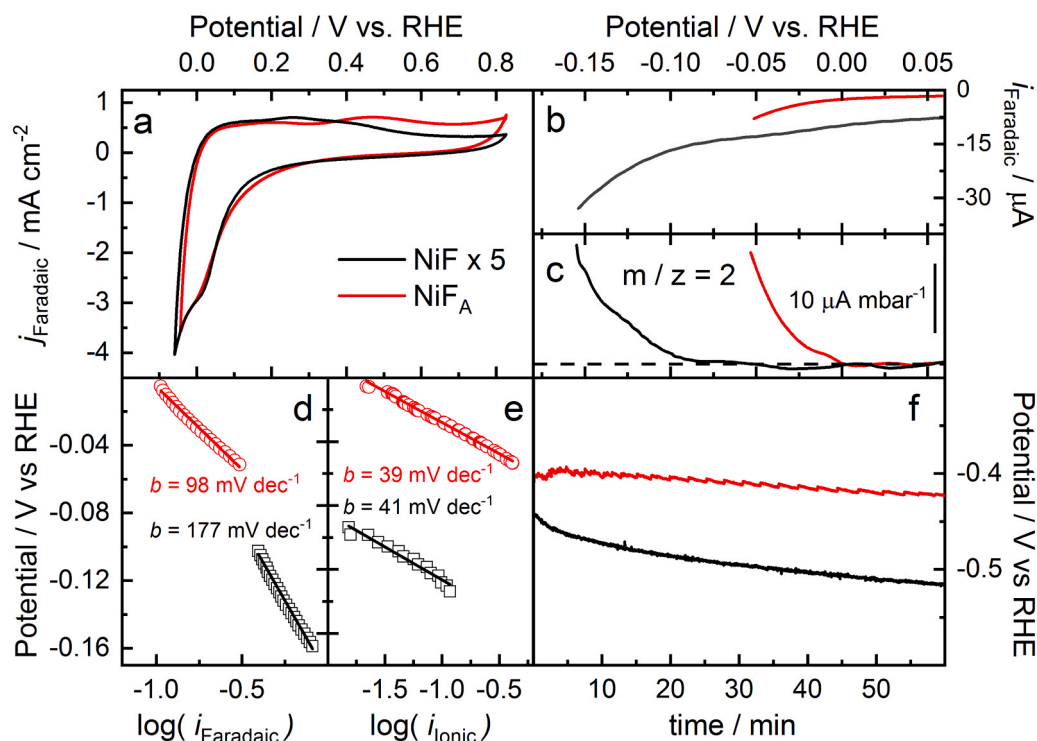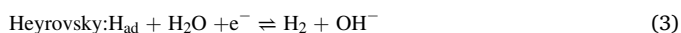
Fig. 6. Cyclic voltammogram recorded at 20 mV s^{-1} (a). Linear sweep voltammogram recorded at 2 mV s^{-1} (b). Mass linear sweep voltammogram recorded at 2 mV s^{-1} (c). Faradaic Tafel plots (d). Ionic Tafel plot (e) and potential transient recorded at 10 mA cm^{-2} (f) for NiF (black lines) and NiF$_A$ (red lines) in 0.1 M NaOH.

reduction [60–62]. To overcome these problems, DEMS was employed, and therefore, accurate onset potentials, kinetics, and mechanistic parameters can be easily attained [60–62].

Linear sweep voltammetry (LSV, Fig. 6b) and mass spectrometer linear sweep voltammetry (MSLSV, Fig. 6c) for the $m/z = 2$ signal (related to H$_2$ formation) in 0.1 M NaOH were employed to study the HER. The working electrode was immersed into the solution at a controlled potential of 0.075 V and the potential was swept in the negative direction at 0.001 V s^{-1}.

LSV of NiF shows cathodic currents along the potential range which are mainly associated with the reduction of surface oxide species observed at IR and Raman spectroscopies. MSLSV signal increases only at lower potentials than 0.09 V. On the other hand, the HER is strongly enhanced at the NiF$_A$ electrode, in which the onset potential developed by the MSLSV is about 10.0 mV (vs. RHE), very close to the thermodynamic value of 0.0 V.

Tafel plots were calculated from LSVs (Fig. 6d) and MSLSVs (Fig. 6e) for NiF (black lines) and NiF$_A$ (red lines) electrodes. Tafel slope values (TS) are usually employed to study reaction kinetics and mechanisms. However, as it was recently reported, TS obtained from faradaic currents is not accurate when studying non-noble materials [60–62]. Indeed, Fig. 6d reveals high and far from theoretical TS when faradaic currents are employed. Hence, faradaic currents are due not only to HER, but also to other by-side reactions such as the electrochemical reduction of surface oxide species, which clarifies the high slope values obtained. On the other hand, TS attained with ionic currents for both catalysts are small and equal to 0.04 V dec^{-1}, this indicates a similar reaction mechanism with the Heyrovsky step (Eq. (3)) as the rate-determining step (RDS):

Volmer: H$_2$O + e$^-$ ⇌ H$_{ad}$ + OH$^-$ (2)

Heyrovsky: H$_{ad}$ + H$_2$O + e$^-$ ⇌ H$_2$ + OH$^-$ (3)

Tafel: H$_{ad}$ + H$_{ad}$ ⇌ H$_2$ (4)

It is important to note that the discrepancy of TS values acquired by ionic and faradaic currents must be founded on the concurrence of other

electrochemical reactions, such as the electroreduction of surface oxide species, occurring at the same potential range as the HER. Therefore, NiF reveals higher TS values than NiF$_A$ when faradaic currents are used, which is in complete agreement with the higher amount of surface oxides observed by IR and Raman techniques. Hence, it becomes clear the great relevance to study the HER mechanism by DEMS, otherwise, a misstatement could be made as was discussed by S. Díaz-Coello et al. [62].

Furthermore, exchange current density obtained from faradaic (j_0) and ionic (j_{0,H_2}) currents reveal diverse situations for both electrodes. Thus, $j_{0,H_2} = 6.22 \ 10^{-5}$ mA cm^{-2} mbar^{-1}, $j_0 = 98.0$ μA cm^{-2} and $j_{0,H_2}/j_0 = 0.001$ mbar^{-1} were achieved for NiF, while $j_{0,H_2} = 0.027$ mA cm^{-2} mbar^{-1}, $j_0 = 120.0$ μA cm^{-2} and $j_{0,H_2}/j_0 = 0.225$ mbar^{-1} were attained for NiF$_A$. The last ratio ($j_{0,H_2}/j_0$) values indicate higher catalytic efficiency towards the HER at NiF$_A$ in comparison to the NiF electrode.

In contrast, Ni surface reports a theoretical exchange current of 6.31 μA cm^{-2} [63], while the classical etching of Ni foam electrode and its raw material report values of 3.9 and 5.9 μA cm^{-2}, respectively [65–67]. As well, Ir-activated nickel foam electrodes report a maximum value of 5.6 μA cm^{-2} in 1.0 M NaOH [66]. This means that the anhydrous etching treatment allows obtaining Pt-free materials with a competitive electroactivity towards HER in comparison to Pt-modified Ni foam (~440 μA cm^{-2}) [64] and 20 wt% Pt/C (~730 μA cm^{-2}) electrocatalysts in alkaline media [68].

On the other hand, the etched surface of NiF$_A$ shows smaller open circuit potential (OCP) than NiF. Furthermore, the electrochemical stability, and therefore the electrocatalytic performance toward the HER at NiF falls during the first 60 min. Indeed, an additional voltage input of c.a. - 0.1 V is necessary to maintain similar H$_2$ production. In contrast, the electrocatalytic performance toward the HER of NiF$_A$ remains almost equal along the time (Fig. 6f).

Interestingly, a high level of noise at the chronopotentiometry test for NiF$_A$ is observed in comparison to NiF, which is attributed to the great catalytic performance toward the HER, and therefore the efficient production of H$_2$ bubbles that disturb de faradaic current signal at

stationary conditions.

3.3.3. Raman spectroelectrochemistry (Raman-SEC)

In-situ Raman spectra of NiF recorded between 0.1 and $-$ 0.3 V reveal four dispersion modes ascribed to α-Ni(OH)$_2$ (black-filled circles) and one to γ-NiOOH lattice at 1220 cm^{-1} (Fig. 7, bottom panel) [26,69]. Also, free H$_2$O molecules at the electrode/electrolyte interface are registered by four Raman-active modes. The first one at ~1650 cm^{-1} is associated with HOH bending mode (δ_{H_2O}) and observed as a shoulder peak close to the 2M_{NiO} mode. Another two signals at 3250 and 3430 cm^{-1} are assigned to symmetric (ν_{s,H_2O}) and asymmetric (ν_{as,H_2O}) stretching mode of water, respectively [70,71]. In addition, a shoulder peak at ~ 3600 cm^{-1} is related to the free OH vibrational mode [71,73].

It is to recall that ex-situ Raman spectrum of NiF shows superficial impurities as a broad band at 2100 and 2880 cm^{-1} ascribed to carbon-based species [53,54]. Indeed, the pretreatment of NiF samples in acetone solution removed most of the organic impurities (see Fig. 5). Hence, the remaining organic impurities are dissolved in the alkaline electrolyte exposing NiO Raman active modes (Fig. 7) [40,63]. Furthermore, the internal NiO$_x$ layer characterized by a broad band at c. a. 2400 cm^{-1} and ascribed to the four magnetic resonances (4 M) of the NiO$_x$ lattice can be discerned at Fig. 7 [58,75–78].

Current transients (Fig. 7, top panel) and Raman spectra (Fig. 7, bottom panel) at different applied potentials, between 0.1 to $-$ 0.3 V with 0.1 V of step potential, were recorded. Interestingly, Raman spectra are almost equal and independent of the applied potential, which indicates that surface species at the NiF electrode remain without apparent changes during the HER.
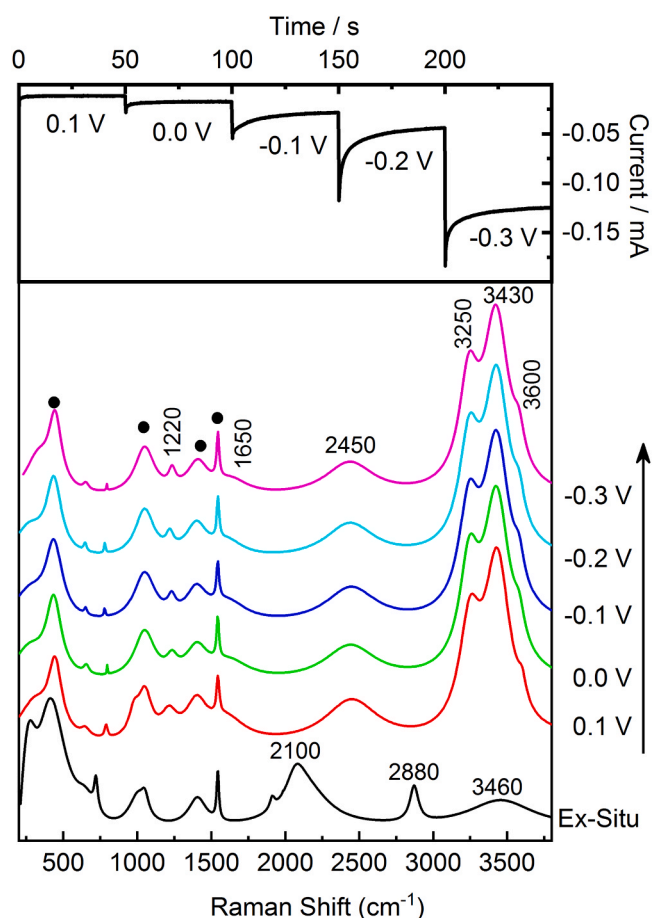
Fig. 8 depicts currents transients (top panel), ex-situ Raman spectra multiplied by a factor of ten (black line, bottom panel), in-situ Raman spectra acquired between 0.1 and $-$ 0.3 V in alkaline media (colored lines, bottom panel) and deconvoluted bands of Raman spectra recorded at 0.1 V (thin orange lines) for NiF$_A$ electrode. The spectrum recorded in the presence of air (i.e., ex-situ) was already described in Fig. 6.

On the other hand, all in-situ spectra reveal two broad peaks centered at ca. 1400 and 3400 cm^{-1} that change with the applied potential, which is completely different from that observed at the NiF electrode (Fig. 7). Furthermore, surface-enhanced Raman scattering (SERS) was discerned when in-situ experiments are performed at the NiF$_A$ electrode, which was not observed at NiF catalyst. The last effect may be ascribed to the etching treatment that produces a rough metal surface with a microstructure array (Fig. 2f) [77,78].

Raman Spectra deconvolution of the spectra recorded at 0.1 V (thin orange lines) reveal 5 and 3 main contributions at the broad peaks observed at lower and higher Raman shifts, respectively. The broad peak at ca. 1400 cm^{-1} involves three signals associated with α-Ni(OH)$_2$ (1050, 1380, and 1550 cm^{-1}), one related to the γ-NiOOH lattice at 1235 cm^{-1} and another one at ~1650 cm^{-1} linked to the bending mode of water (δ_{H_2O}). Meanwhile, the broad contribution peaking at ca. 3400 cm^{-1} comprises three signals associated with stretching modes of water ($\nu_{s,H_2O} = 3200$ cm^{-1} and $\nu_{as,H_2O} = 3245$ cm^{-1}) and to the vibrational mode of free OH$^-$, i.e., the electrolyte.

Interestingly, shifting the potential towards more negative values produces an increment of those species involved in the Raman signal at ca. 1400 cm^{-1}, while the opposite occurs with those implicated in the
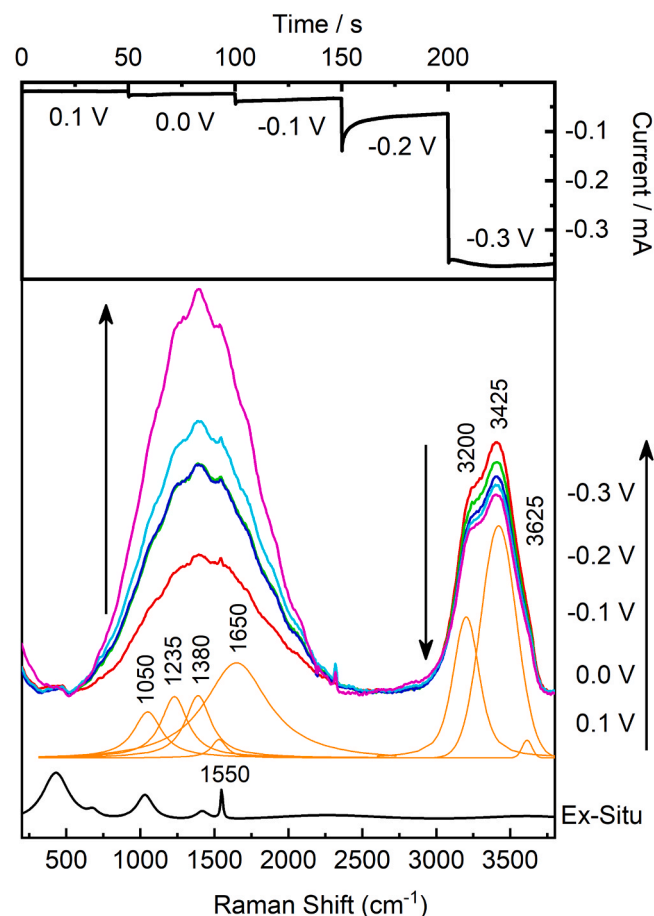

Fig. 7. Current transient (top panel), Raman spectra for NiF catalyst in the presence of air (black line, bottom panel) and in-situ Raman-SEC recorded between 0.1 and $-$ 0.3 V (colored lines) at NiF catalyst in 0.1 M NaOH.

Fig. 8. Current transient (top panel), Raman spectra for NiF$_A$ catalyst in the presence of air (black line x 10, bottom panel), in-situ Raman-SEC recorded between 0.1 and $-$ 0.3 V (colored lines) at NiF$_A$ and deconvoluted lines (orange lines) for the spectra recorded at 0.1 V at NiF$_A$ in 0.1 M NaOH.

broad peak at ca. 3400 cm^{-1}. In other words, stretching modes of water are consumed and adsorbed oxygenated species (i.e., NiO$_x$H$_y$) are produced as the applied potential is more negative.

Therefore, the great difference in the catalytic performance toward the HER at both electrodes can be found in the presence of surface NiO species at NiF (signal at 2450 cm^{-1} in Fig. 7) that may act as passivating species, which are removed after the anhydrous etching treatment. The absence of surface NiO at NiF$_A$ may produce a higher metallic character and, consequently, different spectroelectrochemical behavior in comparison to NiF. In addition to the described above, the higher contraction degree of the NiF$_A$ surface lattice (see Fig. 5) appears as another factor contributing to the great catalytic activity towards the HER in comparison to NiF (see current transients at the top panels of Figs. 7 and 8).

4. Conclusions

Hydrogen evolution reaction (HER) at Ni foam catalysts is enhanced after the anhydrous etching treatment that i) removes organic impurities; ii) rises the crystallinity; iii) eliminates surface passivating species (NiO); and iv) induces surface strain. Indeed, the etched surface exhibits outstanding electroactivity towards HER achieving an onset potential very close to the thermodynamic value of 0.0 V.

Differential electrochemical mass spectrometry (DEMS) and Raman spectroelectrochemistry (Raman-SEC) were used to scrutinize the electrode-electrolyte interface behavior of nickel-based electrodes towards the HER. In this way, the reaction mechanism of the HER was elucidated, and the Heyrovsky step emerged as the rate-determining step (RDS) at both Ni foam-based electrodes.

Furthermore, DEMS appears as a versatile technique to elucidate the kinetic and the mechanism reaction, as well as to precisely determine the onset potential for the HER.

CRediT authorship contribution statement

Conceptualization, **G.G., E.P. and A.M.B-M.**; methodology, **A.B-A. and J.L.R.**; validation, **G.G. and A.M.B-M.**; formal analysis, **G.G.**; data curation, **A.B-A. and J.L.R.**; writing – original draft preparation, **G.G., A.B-A., E.P. and A.M.B-M.**; writing – review and editing, **G.G. and A. M.B-M**; funding acquisition, **G.G., E.P. and A.M.B-M.** All authors have read and agreed to the published version of the manuscript.

Declaration of Competing Interest

The authors declare that they have no known competing financial interests or personal relationships that could have appeared to influence the work reported in this paper.

Data Availability

Data will be made available on request.

Acknowledgments

References

[1] A. Züttel, A. Remhof, A. Borgschulte, O. Friedrichs, Hydrogen: The future energy carrier, Philos. Trans. R. Soc. A Math. Phys. Eng. Sci. 368 (2010) 3329–3342, https://doi.org/10.1098/rsta.2010.0113.

[2] J. Li, J. Hu, M. Zhang, W. Gou, S. Zhang, Z. Chen, Y. Qu, Y. Ma, A fundamental viewpoint on the hydrogen spillover phenomenon of electrocatalytic hydrogen evolution, Nat. Commun. 12 (2021) 1–12, https://doi.org/10.1038/s41467-021-23750-4.

[3] B. Parkinson, J. Turner, Chapter 1: the potential contribution of photoelectrochemistry in the global energy future. Photoelectrochem. Water Split. Mater. Process. Archit 9, The Royal Society of Chemistry,, 2013, pp. 1–18, https://doi.org/10.1039/9781849737739-00001.

[4] M. David, C. Ocampo-Martínez, R. Sánchez-Peña, Advances in alkaline water electrolyzers: A review, J. Energy Storage 23 (2019) 392–403, https://doi.org/10.1016/j.est.2019.03.001.

[5] R.L. Germscheidt, D.E.B. Moreira, R.G. Yoshimura, N.P. Gasbarro, E. Datti, P.L. dos Santos, J.A. Bonacin, Hydrogen environmental benefits depend on the way of production: an overview of the main processes production and challenges by 2050, Adv. Energy Sustain. Res. 2 (2021) 2100093, https://doi.org/10.1002/aesr.202100093.

[6] X. Li, L. Zhao, J. Yu, X. Liu, X. Zhang, H. Liu, W. Zhou, Water splitting: from electrode to green energy system, Nano Micro Lett. 12 (2020) 1–29, https://doi.org/10.1007/s40820-020-00469-3.

[7] C. Santoro, A. Lavacchi, P. Mustarelli, V. Di Noto, L. Elbaz, D.R. Dekel, F. Jaouen, What is next in anion-exchange membrane water electrolyzers? Bottlenecks, benefits, and future, ChemSusChem 15 (2022), e202200027, https://doi.org/10.1002/cssc.202200027.

[8] M. Chatenet, B.G. Pollet, D.R. Dekel, F. Dionigi, J. Deseure, P. Millet, R.D. Braatz, M.Z. Bazant, M. Eikerling, I. Staffell, P. Balcombe, Y. Shao-Horn, H. Schäfer, Water electrolysis: from textbook knowledge to the latest scientific strategies and industrial developments, Chem. Soc. Rev. 51 (2022) 4583–4762, https://doi.org/10.1039/d0cs01079k.

[9] C. Huang, B. Zhang, Y. Wu, Q. Ruan, L. Liu, J. Su, Y. Tang, R. Liu, P.K. Chu, Experimental and theoretical investigation of reconstruction and active phases on honeycombed Ni3N-Co3N/C in water splitting, Appl. Catal. B Environ. 297 (2021), 120461, https://doi.org/10.1016/j.apcatb.2021.120461.

[10] A. Lasia, Mechanism and kinetics of the hydrogen evolution reaction, Int. J. Hydrog. Energy 44 (2019) 19484–19518, https://doi.org/10.1016/j.ijhydene.2019.05.183.

[11] N. Mahmood, Y. Yao, J.W. Zhang, L. Pan, X. Zhang, J.J. Zou, Electrocatalysts for hydrogen evolution in alkaline electrolytes: mechanisms, challenges, and prospective solutions 5 (2018) 1700464, https://doi.org/10.1002/advs.447.

[12] Y. Zheng, Y. Jiao, M. Jaroniec, S.Z. Qiao, Advancing the electrochemistry of the hydrogen- Evolution reaction through combining experiment, Angew. Chem. Int. Ed. 54 (2015) 52–65, https://doi.org/10.1002/anie.201407031.

[13] M. Ďurovič, J. Hnát, K. Bouzek, Electrocatalysts for the hydrogen evolution reaction in alkaline and neutral media. A comparative review, J. Power Sources 493 (2021) 229708, https://doi.org/10.1016/j.jpowsour.2021.229708.

[14] A.S. Aricò, S. Siracusano, N. Briguglio, V. Baglio, A. Di Blasi, A. Antonucci, Polymer electrolyte membrane water electrolysis: Status of technologies and potential applications in combination with renewable power sources, J. Appl. Electrochem. 43 (2013) 107–118, https://doi.org/10.1007/s10800-012-0490-5.

[15] K. Hu, M. Wu, S. Hinokuma, T. Ohto, M. Wakisaka, J.I. Fujita, Y. Ito, Boosting electrochemical water splitting: via ternary NiMoCo hybrid nanowire arrays, J. Mater. Chem. A. 7 (2019) 2156–2164, https://doi.org/10.1039/c8ta11250a.

[16] M. Gong, D.Y. Wang, C.C. Chen, B.J. Hwang, H. Dai, A mini review on nickel-based electrocatalysts for alkaline hydrogen evolution reaction, Nano Res 9 (2016) 28–46, https://doi.org/10.1007/s12274-015-0965-x.

[17] M. Gong, H. Dai, A mini review of NiFe-based materials as highly active oxygen evolution reaction electrocatalysts, Nano Res 8 (2015) 23–39, https://doi.org/10.1007/s12274-014-0591-z.

[18] Y. Gogotsi, R.M. Penner, Energy storage in nanomaterials - capacitive, pseudocapacitive, or battery-like? ACS Nano 12 (2018) 2081–2083, https://doi.org/10.1021/acsnano.8b01914.

[19] D. Huang, S. Li, Y. Luo, L. Liao, J. Ye, H. Chen, Selflated construction of 1D NiMo nanowires: Via a Li electrochemical tuning method for the hydrogen evolution reaction, Nanoscale 11 (2019) 19429–19436, https://doi.org/10.1039/c9nr05311e.

[20] M. Zhiani, F. Jalili, S. Kamali, In situ cathode polarization measurement in alkaline anion exchange membrane water electrolyzer equipped with a PdNiFeCo/C-Ceria hydrogen evolution electrocatalyst, Int. J. Hydrog. Energy 42 (2017) 26563–26574, https://doi.org/10.1016/j.ijhydene.2017.09.038.

[21] A. Eftekhari, Electrocatalysts for hydrogen evolution reaction, Int. J. Hydrog. Energy 42 (2017) 11053–11077, https://doi.org/10.1016/j.ijhydene.2017.02.125.

[22] X. Yu, J. Zhao, L.R. Zheng, Y. Tong, M. Zhang, G. Xu, C. Li, J. Ma, G. Shi, Hydrogen evolution reaction in alkaline media: alpha- or beta-nickel hydroxide on the surface of platinum, ACS Energy Lett. 3 (2018) 237–244, https://doi.org/10.1021/acsenergylett.7b01103.

[23] Y. Yang, D. Wu, R. Li, P. Rao, J. Li, P. Deng, J. Luo, W. Huang, Q. Chen, Z. Kang, Y. Shen, X. Tian, Engineering the strong metal support interaction of titanium nitride and ruthenium nanorods for effective hydrogen evolution reaction, Appl. Catal. B Environ. 317 (2022), 121796, https://doi.org/10.1016/j.apcatb.2022.121796.

[24] U.S. Chavan, P.E. Lokhande, S. Bhosale, Nickel hydroxide nanosheets grown on nickel foam for high performance supercapacitor applications, Mater. Technol. 00 (2021) 1–7, https://doi.org/10.1080/10667857.2021.1873636.

[25] A.A. Hayat, S.K.B. Mane, N. Shaishta, J. Khan, A.A. Hayat, G. Keyum, I. Uddin, F. Raziq, M. Khan, G. Manjunatha, Nickel oxide nano-particles on 3D nickel foam substrate as a non-enzymatic glucose sensor, J. Electrochem. Soc. 166 (2019) B1602–B1611, https://doi.org/10.1149/2.0491915jes.

[26] K. Wan, J. Luo, X. Zhang, P. Subramanian, J. Fransaer, In-situ formation of Ni (oxy) hydroxide on Ni foam as an efficient electrocatalyst for oxygen evolution reaction, Int. J. Hydrog. Energy 45 (2020) 8490–8496, https://doi.org/10.1016/j.ijhydene.2020.01.043.

[27] N.K. Chaudhari, H. Jin, B. Kim, K. Lee, Nanostructured materials on 3D nickel foam as electrocatalysts for water splitting, Nanoscale 9 (2017) 12231–12247, https://doi.org/10.1039/c7nr04187j.

[28] C. Li, J. Hou, Z. Wu, K. Guo, D. Wang, T. Zhai, H. Li, Acid promoted Ni/NiO monolithic electrode for overall water splitting in alkaline medium, Sci. China Mater. 60 (2017) 918–928, https://doi.org/10.1007/s40843-017-9089-y.

[29] W. Zhang, D. Li, L. Zhang, X. She, D. Yang, NiFe-based nanostructures on nickel foam as highly efficiently electrocatalysts for oxygen and hydrogen evolution reactions, J. Energy Chem. 39 (2019) 39–53, https://doi.org/10.1016/j.jechem.2019.01.017.

[30] J. Cao, H. Li, J. Pu, S. Zeng, L. Liu, L. Zhang, F. Luo, L. Ma, K. Zhou, Q. Wei, Hierarchical NiMo alloy microtubes on nickel foam as an efficient electrocatalyst for hydrogen evolution reaction, Int. J. Hydrog. Energy 44 (2019) 24712–24718, https://doi.org/10.1016/j.ijhydene.2019.07.229.

[31] Q. Zhang, P. Li, D. Zhou, Z. Chang, Y. Kuang, X. Sun, Superaerophobic ultrathin Ni–Mo alloy nanosheet array from in situ topotactic reduction for hydrogen evolution reaction, Small 13 (2017) 1721648, https://doi.org/10.1002/smll.201701648.

[32] V. Kovalenko, V. Kotok, I. Kovalenko, Activation of the nickel foam as a current collector for application in supercapacitors, East. -Eur. J. Enterp. Technol. 3 (2018) 56–62, https://doi.org/10.15587/1729-4061.2018.133472.

[33] M. Salavati-Niasari, F. Davar, Z. Fereshteh, Synthesis of nickel and nickel oxide nanoparticles via heat-treatment of simple octanoate precursor, J. Alloy. Compd. 494 (2010) 410–414, https://doi.org/10.1016/j.jallcom.2010.01.063.

[34] S.A. Speakman, Introduction to X-Ray Powder Diffraction Data Analysis, Materials Research Science and Engineering Center, MIT,, 2013, pp. 1–55.

[35] S. He, W. Zhang, L. Liu, Y. Huang, J. He, W. Xie, P. Wu, C. Du, Baseline correction for Raman spectra using an improved asymmetric least squares method, Anal. Methods (2014), https://doi.org/10.1039/c4ay00068d.

[36] R. Gautam, S. Vanga, F. Ariese, S. Umapathy, Review of multidimensional data processing approaches for Raman and infrared spectroscopy, EPJ Tech. Instrum. 2 (2015), https://doi.org/10.1140/epjti/s40485-015-0018-6.

[37] D.S. Hall, D.J. Lockwood, S. Poirier, C. Bock, B.R. MacDougall, Raman and infrared spectroscopy of α and β phases of thin nickel hydroxide films electrochemically formed on nickel, J. Phys. Chem. A. 116 (2012) 6771–6784, https://doi.org/10.1021/jp303546r.

[38] O. Guillén-Villafuerte, G. García, M.C. Arévalo, J.L. Rodríguez, E. Pastor, New insights on the electrochemical oxidation of ethanol on carbon-supported Pt electrode by a novel electrochemical mass spectrometry configuration, Electrochem. Commun. 63 (2016) 48–51, https://doi.org/10.1016/j.elecom.2015.12.007.

[39] L.M. Rivera-Gavidia, M. Luis-Sunga, M. Bousa, V. Vales, M. Kalbac, M.C. Arévalo, E. Pastor, G. García, S- and N-doped graphene-based catalysts for the oxygen evolution reaction, Electrochim. Acta 340 (2020), 135975, https://doi.org/10.1016/j.electacta.2020.135975.

[40] M. Grdeń, M. Alsabet, G. Jerkiewicz, Surface science and electrochemical analysis of nickel foams, ACS Appl. Mater. Interfaces 4 (2012) 3012–3021, https://doi.org/10.1021/am300380m.

[41] W. Lai, L. Ge, H. Li, Y. Deng, B. Xu, B. Ouyang, E. Kan, In situ Raman spectroscopic study towards the growth and excellent HER catalysis of Ni/Ni(OH)2 heterostructure, Int. J. Hydrog. Energy 46 (2021) 26861–26872, https://doi.org/10.1016/j.ijhydene.2021.05.158.

[42] D.S. Hall, D.J. Lockwood, C. Bock, B.R. MacDougall, Nickel hydroxides and related materials: A review of their structures, synthesis and properties, Proc. R. Soc. A Math. Phys. Eng. Sci. 471 (2015), https://doi.org/10.1098/rspa.2014.0792.

[43] S.L. Medway, C.A. Lucas, A. Kowal, R.J. Nichols, D. Johnson, In-situ studies of the oxidation of nickel electrodes in alkaline solution, J. Electroanal. Chem. 587 (2006) 172–181, https://doi.org/10.1016/j.jelechem.2005.11.013.

[44] G. Chen, T. Wang, J. Zhang, P. Liu, H. Sun, X. Zhuang, M. Chen, X. Feng, Accelerated hydrogen evolution kinetics on NiFe-layered double hydroxide electrocatalysts by tailoring water dissociation active sites (1-7), Adv. Mater. 30 (2018) 1706279, https://doi.org/10.1002/adma.201706279.

[45] S.A. Speakman, Basics of X-Ray Powder Diffraction, Materials Research Science and Engineering Center, Massachusetts Institute of Technology (MIT),, 2012, pp. 1–107 (Available from), ⟨http://prism.mit.edu/xray/documents/1%20Basics%20of%20X-Ray%20Powder%20Diffraction.pdf⟩.

[46] J. Lu, T. Xiong, W. Zhou, L. Yang, Z. Tang, S. Chen, Metal nickel foam as an efficient and stable electrode for hydrogen evolution reaction in acidic electrolyte under reasonable overpotentials, ACS Appl. Mater. Interfaces 8 (2016) 5065–5069, https://doi.org/10.1021/acsami.6b00233.

[47] G. García, J.A. Silva-Chong, O. Guillén-Villafuerte, J.L. Rodríguez, E.R. González, E. Pastor, CO tolerant catalysts for PEM fuel cells Spectroelectrochemical studies, Catal. Today 116 (2006) 415–421, https://doi.org/10.1016/j.cattod.2006.05.069.

[48] Y. Mao, B. Zhou, S. Peng, Simple deposition of mixed α, β-nickel hydroxide thin film onto nickel foam as high-performance supercapacitor electrode material, J. Mater. Sci. Mater. Electron. 31 (2020) 9457–9467, https://doi.org/10.1007/s10854-020-03485-6.

[49] M. Aghazadeh, A.N. Golikand, M. Ghaemi, Synthesis, characterization, and electrochemical properties of ultrafine β-Ni(OH)2 nanoparticles, Int. J. Hydrog. Energy 36 (2011) 8674–8679, https://doi.org/10.1016/j.ijhydene.2011.03.144.

[50] V. Paserin, S. Marcuson, J. Shu, D.S. Wilkinson, CVD technique for inco nickel foam production, Adv. Eng. Mater. 6 (2004) 454–459, https://doi.org/10.1002/adem.200405142.

[51] O.B. Olurin, D.S. Wilkinson, G.C. Weatherly, V. Paserin, J. Shu, Strength and ductility of as-plated and sintered CVD nickel foams, Compos. Sci. Technol. 63 (2003) 2317–2329, https://doi.org/10.1016/S0266-3538(03)00265-3.

[52] D.S. Hall, D.J. Lockwood, S. Poirier, C. Bock, B.R. MacDougall, Applications of in situ Raman spectroscopy for identifying nickel hydroxide materials and surface layers during chemical aging, ACS Appl. Mater. Interfaces 6 (2014) 3141–3149, https://doi.org/10.1021/am405419h.

[53] C.S. Casari, A. Li Bassi, A. Baserga, L. Ravagnan, P. Piseri, C. Lenardi, M. Tommasini, A. Milani, D. Fazzi, C.E. Bottani, P. Milani, Low-frequency modes in the Raman spectrum of sp-s p2 nanostructured carbon, Phys. Rev. B - Condens. Matter Mater. Phys. 77 (2008), https://doi.org/10.1103/PhysRevB.77.195444.

[54] Horiba Jobin Yvon company (HORIBA), Raman Spectroscopy for Analysis and Monitoring, Horiba Jobin Yvon - Raman Application Note. (2017) 1–2. Available from: https://static.horiba.com/fileadmin/Horiba/Technology/Measurement_Techniques/Molecular_Spectroscopy/Raman_Spectroscopy/Raman_Academy/Raman_Tutorial/Raman_bands.pdf. No subcribtion required.

[55] J. Liang, Y.Z. Wang, C.C. Wang, S.Y. Lu, In situ formation of NiO on Ni foam prepared with a novel leaven dough method as an outstanding electrocatalyst for oxygen evolution reactions, J. Mater. Chem. A. 4 (2016) 9797–9806, https://doi.org/10.1039/c6ta03729a.

[56] J. Babjak, V.A. Ettel, V. Paserin. Method of forming nickel foam. US Patent 4957543A. 1990–09-18. Pages 1–6. Available from: patents.google.com/patent/US4957543A/en.

[57] N. Mironova-Ulmane, A. Kuzmin, I. Steins, J. Grabis, I. Sildos, M. Pärs, Raman scattering in nanosized nickel oxide NiO, J. Phys. Conf. Ser. 93 (2007), https://doi.org/10.1088/1742-6596/93/1/012039.

[58] N. Mironova-Ulmane, A. Kuzmin, I. Sildos, M. Pärs, Polarisation dependent Raman study of single-crystal nickel oxide, Cent. Eur. J. Phys. 9 (2011) 1096–1099, https://doi.org/10.2478/s11534-010-0130-9.

[59] F. Hahn, D. Floner, B. Beden, C. Lamy, In-situ investigation of the behaviour of a nickel electrode in alkaline solution by uv–vis and ir reflectance spectroscopies, Electrochim. Acta 32 (1987) 1631–1636, https://doi.org/10.1016/0013-4686(87)90016-8.

[60] S. Díaz-Coello, J.A. Palenzuela, M.M. Afonso, E. Pastor, G. García, WC modified with ionic liquids for the hydrogen evolution reaction in alkaline solution, J. Electroanal. Chem. 880 (2021) 114878, https://doi.org/10.1016/j.jelechem.2020.114878.

[61] S. Díaz-Coello, M.M. Afonso, J.A. Palenzuela, E. Pastor, G. García, Composite materials from transition metal carbides and ionic liquids as electrocatalyst for hydrogen evolution in alkaline media, J. Electroanal. Chem. 898 (2021) 115620, https://doi.org/10.1016/j.jelechem.2021.115620.

[62] S. Díaz-Coello, G. García, M.C. Arévalo, E. Pastor, Precise determination of Tafel slopes by DEMS. Hydrogen evolution on tungsten-based catalysts in alkaline solution, Int. J. Hydrog. Energy 44 (2019), https://doi.org/10.1016/j.ijhydene.2019.02.151.

[63] D.S. Hall, C. Bock, B.R. MacDougall, The electrochemistry of metallic nickel: oxides, hydroxides, hydrides and alkaline hydrogen evolution, J. Electrochem. Soc. 160 (2013) F235–F243, https://doi.org/10.1149/2.026303jes.

[64] J.K. Nørskov, T. Bligaard, A. Logadottir, J.R. Kitchin, J.G. Chen, S. Pandelov, U. Stimming, Trends in the exchange current for hydrogen evolution, J. Electrochem. Soc. 152 (2005) J23–J26, https://doi.org/10.1149/1.1856988.

[65] T. Mikolajczyk, B. Pierozynski, Influence of electrodeposited Ni-Mo alloy on hydrogen evolution reaction at nickel foam cathode, Int. J. Electrochem. Sci. 13 (2018) 621–630, https://doi.org/10.20964/2018.01.68.

[66] M. Luba, T. Mikolajczyk, B. Pierozynski, Hydrogen evolution reaction on iridium-modified nickel foam surfaces, Electrocatalysis 11 (2020) 347–353, https://doi.org/10.1007/s12678-020-00593-z.

[67] B. Pierozynski, T. Mikolajczyk, Cathodic evolution of hydrogen on platinum-modified nickel foam catalyst, Electrocatalysis 7 (2015) 121–126, https://doi.org/10.1007/s12678-015-0290-x.

[68] T. Sun, L. Xu, Y. Yan, A.A. Zakhidov, R.H. Baughman, J. Chen, Ordered mesoporous nickel sphere arrays for highly efficient electrocatalytic water oxidation, ACS Catal. 6 (2016) 1446–1450, https://doi.org/10.1021/acscatal.5b02571.

[69] C. Johnston, P.R. Graves, In situ Raman spectroscopy study of the nickel oxyhydroxide electrode (NOE) system, Appl. Spectrosc. 44 (1990) 105–115, https://doi.org/10.1366/0003702904085769.

[70] A.A. Kananenka, J.L. Skinner, Fermi resonance in OH-stretch vibrational spectroscopy of liquid water and the water hexamer, J. Chem. Phys. 148 (2018), https://doi.org/10.1063/1.5037113.

[71] W.A. Senior, W.K. Thompson, Assignment of the Infra-red and Raman Bands of Liquid Water, Nature 205 (1965) 170, https://doi.org/10.1038/205170a0.

[72] C.D. Shaffer, Quantification of hydroxide in aqueous solutions by Raman spectroscopy, Univ. North Tex. Libr. 1 (1997) 1–24. Resource key: ark:/67531/metadc691791.

[73] J. Stefanski, C. Schmidt, S. Jahn, Aqueous sodium hydroxide (NaOH) solutions at high pressure and temperature: Insights from: In situ Raman spectroscopy and ab initio molecular dynamics simulations, Phys. Chem. Chem. Phys. 20 (2018) 21629–21639, https://doi.org/10.1039/c8cp00376a.

[74] N. Mironova-Ulmane, A. Kuzmin, I. Sildos, L. Puust, J. Grabis, Magnon and phonon excitations in nanosized NiO, Latv. J. Phys. Tech. Sci. 56 (2019) 61–72, https://doi.org/10.2478/lpts-2019-0014.

[75] Z. Szklarska-Smialowska, M. Smialowski, Electrochemical study of the nickel-hydrogen system, J. Electrochem. Soc. 110 (1963) 444, https://doi.org/10.1149/1.2425783.

[76] D.S. Hall, C. Bock, B.R. MacDougall, Surface layers in alkaline media: nickel hydrides on metallic nickel electrodes, ECS Trans. 50 (2013) 165–179, https://doi.org/10.1149/05031.0165ecst.

[77] Y. Zhilin, W.U. Deyin, J. Yao, H.U. Jianqiang, R. Bin, Z. Haiguang, Tian Zhongqun, SERS mechanism of nickel electrode, Chin. Sci. Bull. 47 (2002) 1983–1986, https://doi.org/10.1360/02tb9430.

[78] J.L. Yao, J. Tang, D.Y. Wu, D.M. Sun, K.H. Xue, B. Ren, B.W. Mao, Z.Q. Tian, Surface enhanced Raman scattering from transition metal nano-wire array and the theoretical consideration, Surf. Sci. 514 (2002) 108–116, https://doi.org/10.1016/S0039-6028(02)01615-1.

[79] H. Radinger, P. Connor, S. Tengeler, R.W. Stark, W. Jaegermann, B. Kaiser, Importance of nickel oxide lattice defects for efficient oxygen evolution reaction, Chem. Mater. 33 (2021) 8259–8266, https://doi.org/10.1021/acs.chemmater.1c02406.